GEOPHYSICAL RESEARCH LETTERS

Supporting Information for

Double reservoirs imaged below Great Sitkin Volcano, Alaska, explain the migration of volcanic seismicity

Xiaotao Yang[1], Diana C. Roman[2], Matt Haney[3], Cody A. Kupres[1]

[1]Department of Earth, Atmospheric, and Planetary Sciences, Purdue University, West Lafayette, IN, USA.

[2]Earth and Planets Laboratory, Carnegie Institution for Science, Washington, DC, USA

[3]Alaska Volcano Observatory, USGS, Anchorage, AK, USA

Contents of this file

Introduction

This supplementary file contains additional text and figures to support the main text, including resolution test results, absolute velocity cross-sections, and comparison with the reference model.

Text S1. Resolution analysis

Overall, the final shear-wave velocity model from the full-wave ambient noise tomography is greatly improved compared to the reference model, showing more details below the volcanic island (Figure S2). The maximum resolvable depth is determined by the array's aperture (nominally about 10 km). However, limited by the sparse station coverage, we could only resolve seismic features at a horizontal scale of about 3.5 km and above within the top 5-6 km (Figures S3 and S4a-S4b). Figure S4c-S4d in the supplement shows that the overall geometry of L1 can be recovered with about 20-30% amplitude recovery above the depth of 5 km. The velocity anomalies below the depth of about 5 km, including the low-velocity L2, are mainly carried from

the reference model (Figure S2a-S2c in the supplement) and are poorly resolved by the current data coverage. In terms of amplitudes of the anomalies, we could resolve about 20% of the input velocity perturbation in the top 3-4 km, decreasing to about 10-15% at greater depths. This suggests that while the key relative velocity perturbation patterns could be resolved at a scale of 3.5 km and above, the amplitudes of the velocity anomaly might be greatly underestimated. The underestimation of the perturbation amplitudes is partly due to the damping and smoothing operations as needed to stabilize the inversion process. Informed by the resolution test results, we limit our discussion to those velocity features with a horizontal scale of >3.5 km and a vertical scale of > 2 km.

Text S2. Minor contributions to shear-wave velocity reduction from no-melt mechanisms

The contribution of a temperature anomaly and active fractures to the reduction of shear-wave velocity is negligible. The surface heat flow at the Great Sitkin island, with a sample location northwest of the edifice, is about 97 mW/m^2, similar to the measurements at most of the active Alaska volcanoes (Batir et al., 2016; Batir, 2017). With only one data point, we don't have control over the lateral variation of the surface heat flow and subsurface temperature anomalies across the island. Some geothermal features, including fumaroles, mud pots, and hot springs, are only observed at the southern flank of the edifice, away from the imaged low-velocity anomalies. The reduction of shear-wave velocities is about 0.5% per 100°C relative to the average shear velocity of 3.65 km/s for a variety of dry rock types (Kern et al., 2001). To fully account for the 10% velocity reduction for L1 and L2 anomalies, with a surface temperature of 20°C, the estimated temperature anomaly would be about 2000°C, which is unrealistically

high and is much higher than the melting temperature for minerals in the dry andesite. Even with an extremely high geothermal gradient of 100°C/km as in some active volcanoes (Lowell et al., 2014), the temperature at 4 km depth would be 420°C. This is about 300°C higher than the temperature computed with a geothermal gradient of 25°C/km, contributing to about 1.5% shear-wave velocity reduction. On the other hand, the lack of earthquakes within the imaged low-velocity anomalies rules out the existence of active fractures as a major contribution.

Text S3. Parameters in estimating the melt fractions for L1 and L2 low-velocity anomalies

At the Great Sitkin island, the volcanic deposits are dominantly andesite and basaltic andesite (Miller et al., 1998; Loewen, 2021). Following the procedures and computer codes by Paulatto et al. (2022), we compute the melt fractions for the L1 and L2 low-velocity anomalies (Figure S5). The shear-wave velocity ranges for L1 (1.5-2.1 km/s) and L2 (2.2-2.6 km/s) are estimated between 2-4 km depth and 4-5.5 km depth, respectively, from Figure S1a. We use the Python Jupyter notebook by Paulatto et al. (2022) to compute the melt fraction curves modified for andesite at a depth of 4 km with a density of 2.627 g/cm^3 (about the pressure of 100 MPa). We use 5.445 km/s and 3.005 km/s as the P- and S-wave velocities, respectively, for andesite crystals, as extrapolated based on a second-order polynomial fit of the values in Christensen and Stanley (2003). For dry molten andesite rocks, we use a density of 2.55 g/cm^3 and a P-wave velocity of 2.594 km/s, scaled down from the value by Ueki and Iwamori (2016) at 1 GPa. S-wave velocity is zero for the pure melt. We use two methods, the Self-Consistent Scheme method (Figure S5a) (e.g, Berryman, 1998; Paulatto et al., 2022) and the Differential Effective Medium method (Figure S5b) (e.g., Norris, 1985; Avellaneda, 1987; Paulatto et al., 2022), to

estimate the uncertainties in melt fractions. We compute the melt fractions with a range of spheroidal melt inclusion aspect ratios for dry andesite. We adopt the aspect ratio of 0.1-0.15 (Takei, 2002) to calculate the most probable range of the melt fractions associated with the L1 and L2 anomalies. The melt fractions are about 0.23±0.1 and about 0.11±0.05 for the L1 and L2 anomalies, respectively.

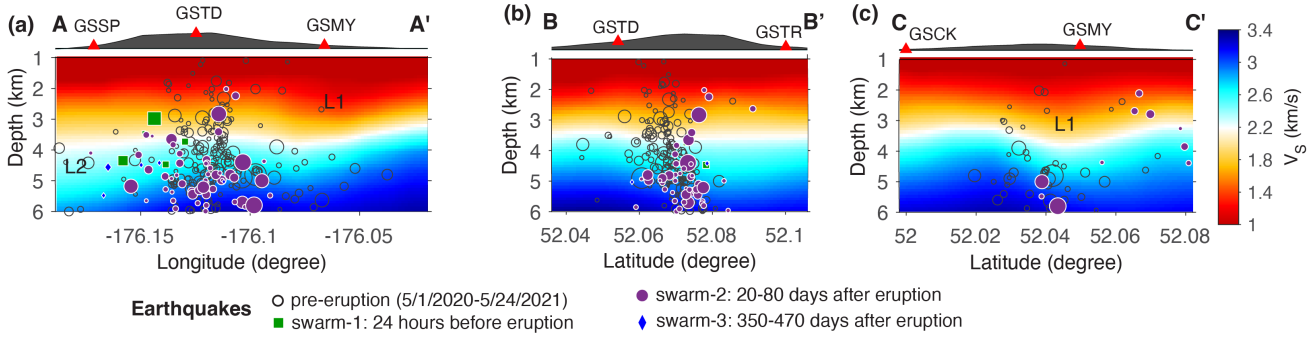

Figure S1. Vertical cross-sections of the shear-wave velocity model between 1-6 km depths showing the absolute velocities. Gray circles are magnitude ≥ 0 earthquakes between 5/1/2020 and 5/24/2021, projected within about 2 km of each profile. Earthquake swarms associated with the 5/26/2021 eruption are also projected with the same parameter. See Figure 2c in the main text for profile locations.

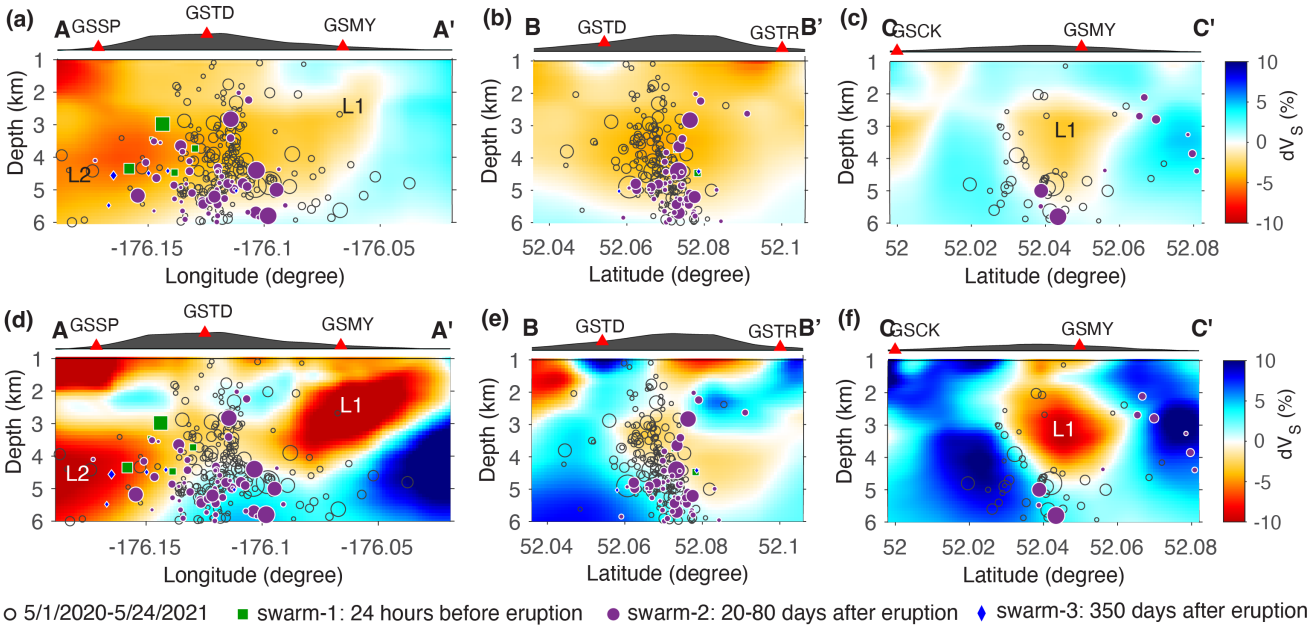

Figure S2. Comparison of cross-sections between the reference velocity model (top) and the final model by this study. The projected earthquakes are the same as in Figure S1. See Figure 2c in the main text for profile locations.

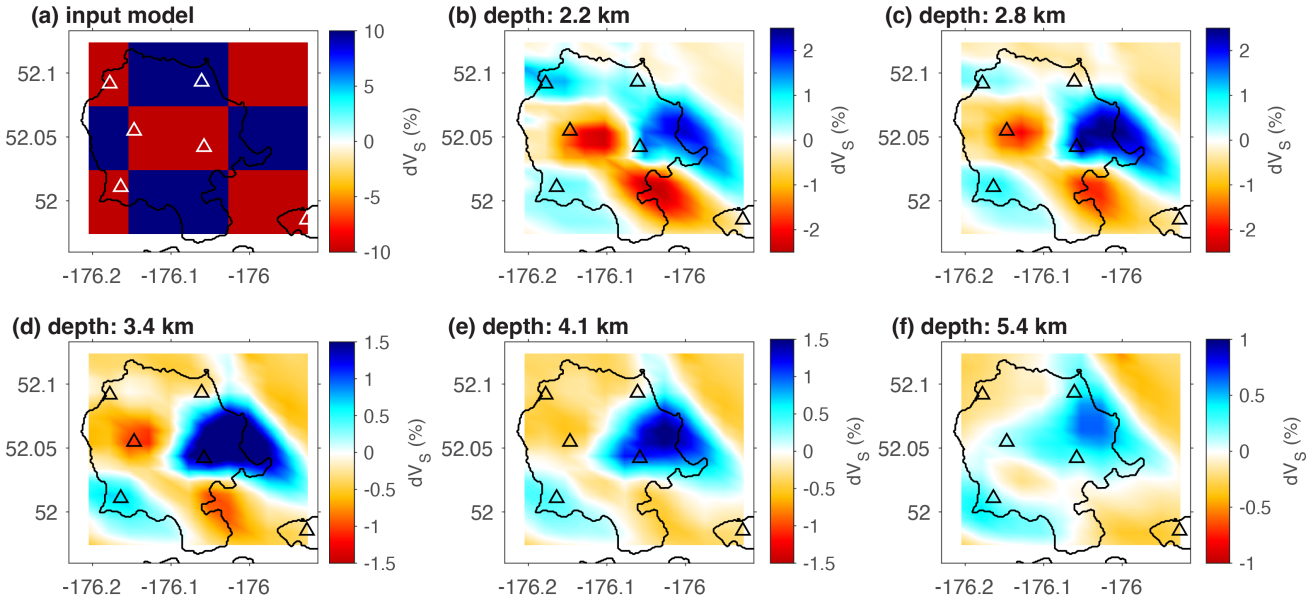

Figure S3. Checkerboard resolution test results. (a) Input checkerboard model at all depths with a perturbation of ±10%. (b)-(f) Recovered checkerboard results with the input model in (a) at depths of (b) 2.2 km, (c) 2.8 km, (d) 3.4 km, (e) 4.1 km, and (f) 5.4 km. The triangles are the seismic stations. Different color ranges are chosen in (b)-(f) to highlight the recovered checkerboard patterns.

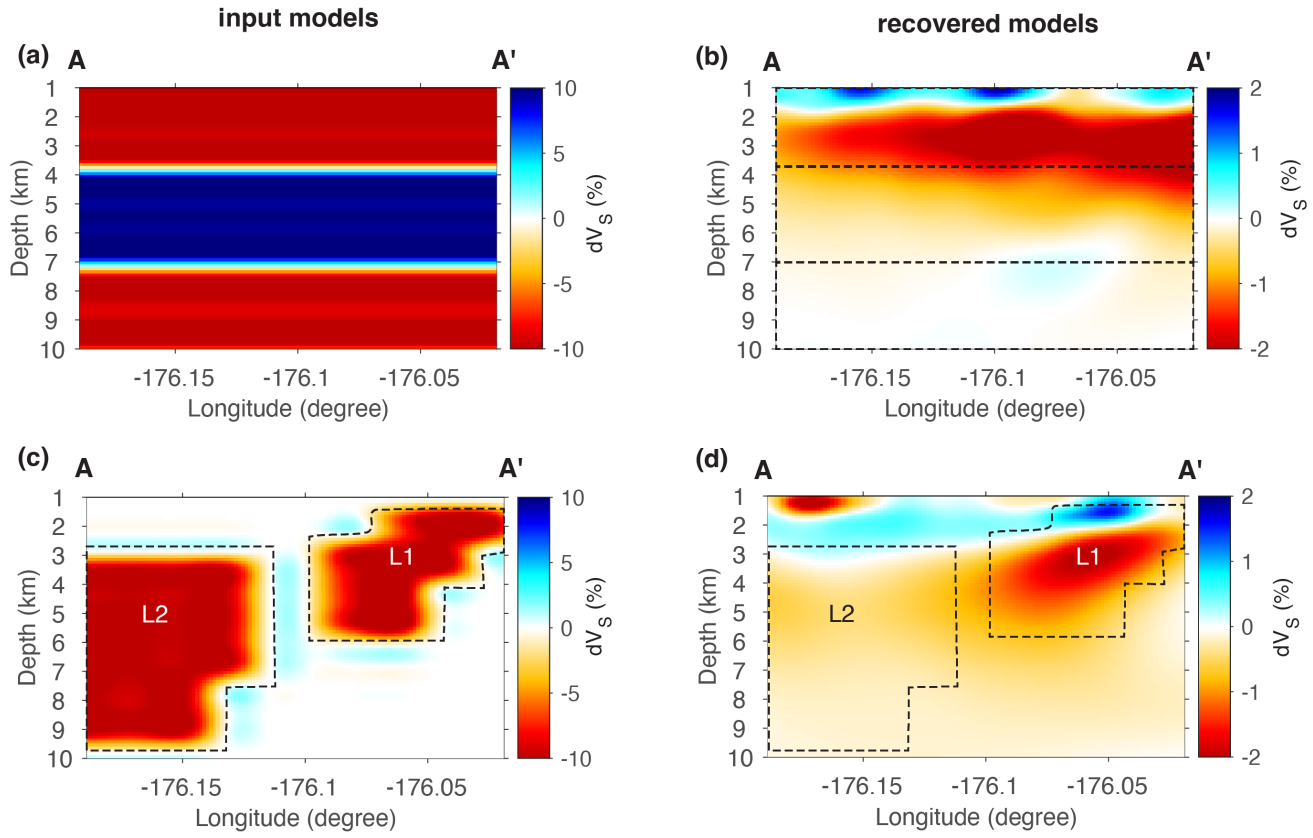

Figure S4. Recovery test results with input models on the left and recovered models on the right. (a-b) A layered model with a thickness of about 3.5 km. (c-d) Results for input low-velocity anomalies simulating the two low-velocity anomalies (L1 and L2) observed in Figure 2d in the main text.

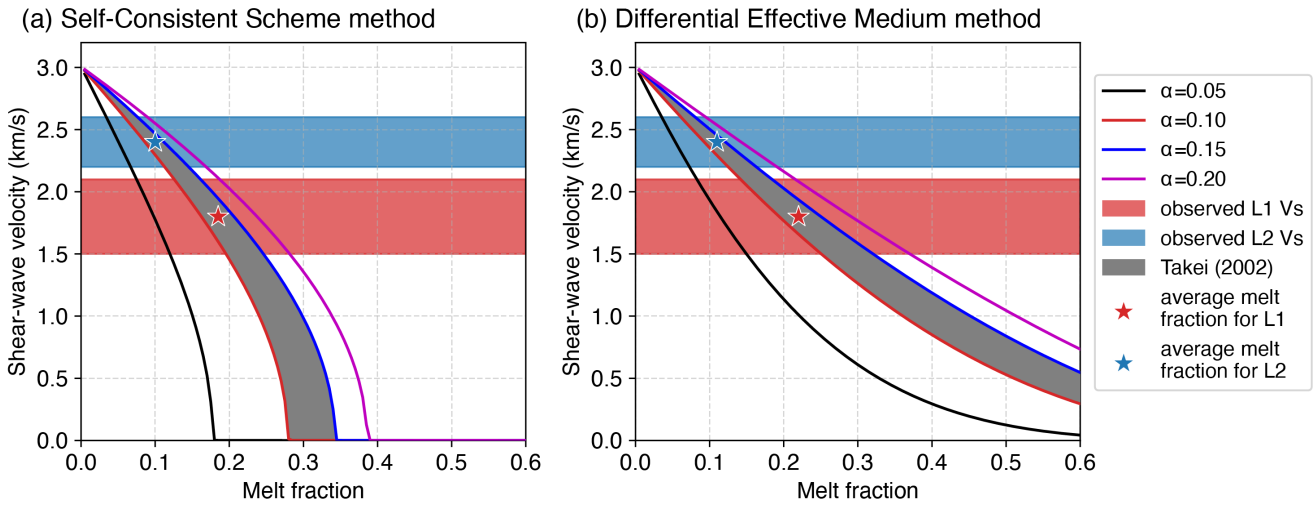

Figure S5. Estimates of the andesite melt fractions for L1 (red star) and L2 (blue star) low-velocity anomalies using two different methods. (a) The relationship between melt fraction and shear-wave velocities estimated using the Self-Consistent Scheme method (e.g, Berryman, 1998; Paulatto et al., 2022). (b) Same as (a) but using the Differential Effective Medium method (e.g., Norris, 1985; Avellaneda, 1987; Paulatto et al., 2022). The curves in (a-b) are color-coded by the aspect ratios (α) of the spheroidal melt inclusions. The gray shaded area marks the aspect ratios suggested by Takei (2002). The red and blue shaded areas mark the ranges of shear-wave velocities for L1 and L2 anomalies, respectively.

References

Avellaneda, M. (1987, 9). Iterated homogenization, differential effective medium theory and applications. *Communications on Pure and Applied Mathematics*, *40*, 527-554. Retrieved from https://onlinelibrary.wiley.com/doi/full/10.1002/cpa.3160400502 doi: 10.1002/CPA.3160400502

Batir, J. F. (2017). *Thermal studies of alaska and british columbia: Examining thermotectonic provinces, climate change, and crustal evolution* (PhD Dissertation, Southern Methodist University). Retrieved from https://www.proquest.com/dissertations-theses/thermal-studies-alaska-british-columbia-examining/docview/1917413401/se-2

Batir, J. F., Blackwell, D. D., & Richards, M. C. (2016). Heat flow and temperature-depth curves throughout alaska: Finding regions for future geothermal exploration. *Journal of Geophysics and Engineering*, *13*, 366-377. doi: 10.1088/1742-2132/13/3/366

Berryman, J. G. (1998, 6). Long-wavelength propagation in composite elastic media ii. ellipsoidal inclusions. *The Journal of the Acoustical Society of America*, *68*, 1820. Retrieved from https://asa.scitation.org/doi/abs/10.1121/1.385172 doi: 10.1121/1.385172

Christensen, N. I., & Stanley, D. (2003). Seismic velocities and densities of rocks. *International Geophysics*, *81*, 1587-1594. doi: 10.1016/S0074-6142(03)80278-4

Kern, H., Popp, T., Gorbatsevich, F., Zharikov, A., Lobanov, K., & Smirnov, Y. (2001, 8). Pressure and temperature dependence of v_p and v_s in rocks from the superdeep well and from surface analogues at kola and the nature of velocity anisotropy. *Tectonophysics*, *338*, 113-134. Retrieved from https://linkinghub.elsevier.com/retrieve/pii/S0040195101001287 doi: 10.1016/S0040-1951(01)00128-7

Loewen, M. W. (2021). *Thin section crossed-polarized light photomicrograph of a radial plagioclase phenocryst in a May 25, 2021, Great Sitkin breadcrust bomb.* Alaska Volcano Observatory / U.S. Geological Survey. Retrieved from https://avo.alaska.edu/images/image.php?id=178421

Lowell, R., Kolandaivelu, K., & Rona, P. (2014). Hydrothermal activity. In *Reference module in earth systems and environmental sciences.* Elsevier. Retrieved from https://www.sciencedirect.com/science/article/pii/B9780124095489091326 doi: https://doi.org/10.1016/B978-0-12-409548-9.09132-6

Miller, T. P., McGimsey, R. G., Richter, D. H., Riehle, J. R., Nye, C., Yount, M. E., & Dumoulin, J. A. (1998). Catalog of the historically active volcanoes of Alaska. *Open-File Report*. doi: 10.3133/OFR98582

Norris, A. (1985, 3). A differential scheme for the effective moduli of composites. *Mechanics of Materials*, *4*, 1-16. Retrieved from https://linkinghub.elsevier.com/retrieve/pii/0167663685900002X doi: 10.1016/0167-6636(85)90002-X

Paulatto, M., Hooft, E. E. E., Chrapkiewicz, K., Heath, B., Toomey, D. R., & Morgan, J. V. (2022, 10). Advances in seismic imaging of magma and crystal mush. *Frontiers in Earth Science*, *10*, 2005. Retrieved from https://www.frontiersin.org/articles/10.3389/feart.2022.970131/full doi: 10.3389/feart.2022.970131

Takei, Y. (2002, 2). Effect of pore geometry on V_P/V_S: From equilibrium geometry to crack. *Journal of Geophysical Research: Solid Earth*, *107*, ECV 6-1. Retrieved from https://onlinelibrary.wiley.com/doi/full/10.1029/2001JB000522https://onlinelibrary.wiley.com/doi/abs/10.1029/2001JB000522https://agupubs

.onlinelibrary.wiley.com/doi/10.1029/2001JB000522 doi: 10.1029/2001JB000522

Ueki, K., & Iwamori, H. (2016, 5). Density and seismic velocity of hydrous melts under crustal and upper mantle conditions. *Geochemistry, Geophysics, Geosystems*, *17*, 1799-1814. Retrieved from https://onlinelibrary.wiley.com/doi/full/10.1002/2015GC006242https://onlinelibrary.wiley.com/doi/abs/10.1002/2015GC006242https://agupubs.onlinelibrary.wiley.com/doi/10.1002/2015GC006242 doi: 10.1002/2015GC006242